ELSEVIER

Hall magnetohydrodynamics on block-adaptive grids

Gábor Tóth [*], Yingjuan Ma, Tamas I. Gombosi

Center for Space Environment Modeling, University of Michigan, Ann Arbor, MI 48109-2143, United States

Abstract

We present a conservative second order accurate finite volume discretization of the magnetohydrodynamics equations including the Hall term. The scheme is generalized to three-dimensional block-adaptive grids with Cartesian or generalized coordinates. The second order accurate discretization of the Hall term at grid resolution changes is described in detail. Both explicit and implicit time integration schemes are developed. The stability of the explicit time integration is ensured by including the whistler wave speed for the shortest discrete wave length into the numerical dissipation, but then second order accuracy requires the use of symmetric limiters in the total variation diminishing scheme. The implicit scheme employs a Newton–Krylov–Schwarz type approach, and can achieve significantly better efficiency than the explicit scheme with an appropriate preconditioner. The second order accuracy of the scheme is verified by numerical tests. The parallel scaling and robustness are demonstrated by three-dimensional simulations of planetary magnetospheres.
© 2008 Elsevier Inc. All rights reserved.

Keywords: Numerical approximation; Magnetohydrodynamics; Numerical methods; Hall MHD; Adaptive grid; Block-adaptive grid

1. Introduction

Ideal or resistive magnetohydrodynamics (MHD) provides a fairly accurate physical model for a wide range of laboratory and space plasma problems. In certain applications, however, some of the MHD approximations become invalid, and the simulations deviate from physical reality. An essential example is reconnection of the magnetic field. Flows around unmagnetized planets and moons also show features, such as asymmetry of the pile-up boundary, that cannot be modeled with classical MHD.

One option to better describe the physics is using full or hybrid particle schemes (see e.g. [3]). While particle and hybrid schemes can successfully model these problems, these algorithms are very costly, especially for three-dimensional (and possibly time dependent) simulations. An alternative approach is to maintain the fluid description of the plasma but allow for the decoupling of the ion and electron fluids.

The Hall term is part of the generalized Ohm's law and it describes the relative speed between ions and electrons. The magnetic field lines are frozen in the electron fluid, but not in the ion fluid due to the Hall effect. The

[*] Corresponding author. Tel.: +1 734 615 5362; fax: +1 734 615 9723.
E-mail address: gtoth@umich.edu (G. Tóth).

Hall effect is important at length scales shorter than the ion skin depth. Including the Hall term modifies the induction equation and the total energy density equation of MHD.

Hall MHD seems to be the minimal modification required to reproduce the fast reconnection process successfully modeled by particle and hybrid schemes [3]. In terms of magnetospheric physics, it is found that the Hall effect is important for both the dayside magnetopause [13] and the nightside magnetotail [14].

Modeling the magnetic reconnection by various methods has been studied in detail for the Geospace Environment Modeling Challenge [3,25,16]. For this non-driven reconnection problem the reconnection rate increases as the Hall parameter is increased. On the other hand [12], found that for externally driven magnetic reconnection the presence of the Hall current does not necessarily enhance the total reconnected flux.

In this paper, we describe a finite volume Hall MHD scheme on a three-dimensional block-adaptive Cartesian or generalized coordinate grid with both explicit and implicit time discretization. To put our work in context, we briefly describe some of the published Hall MHD schemes that are similar to our effort. There are many codes that use relatively simple numerical techniques (e.g. explicit time integration with hyper-resistivity) on structured two-dimensional grids. These schemes would not be efficient for three-dimensional calculations and do not generalize to adaptive grids. Three-dimensional Hall MHD has been successfully modeled by pseudo-spectral codes (e.g. [11,5]), but spectral schemes are not suitable for adaptive grids. The VooDoo code by Huba [7,8] is a three-dimensional high order finite volume scheme using a gas kinetic type flux function and explicit time discretization with subcycling for the Hall physics. We use a similar finite volume approach for the spatial discretization, but use different flux functions and we use implicit time integration scheme instead of subcycling. Chacon and Knoll [4] have developed an implicit scheme for the incompressible Hall MHD equations in two dimensions. Our time integration scheme is similar, but the formulation of the MHD equations is quite different, since we use the usual MHD variables, while Chacon and Knoll use the vector potential and the stream and vorticity functions. The preconditioner is also quite different. Probably the closest to our effort is the recently developed Magnetic Reconnection Code (MRC) [2], a massively parallel Hall MHD code with a patch based adaptive mesh refinement, CWENO type numerical flux, and Newton–Krylov type (semi-)implicit time integration scheme. In the published papers known to us, MRC has been applied to the Hall MHD equations in two dimensions.

We develop a parallel, explicit and/or implicit three-dimensional Hall MHD scheme and implement it into the BATSRUS code [17]. BATSRUS solves the MHD equations with second order shock-capturing total variation diminishing (TVD) schemes on a block-adaptive grid. Block-adaptive grids [19] consist of self-similar blocks as shown in Fig. 1. Each block has a simple logically Cartesian geometry. The grid is refined by dividing a block into 8 smaller blocks, while coarsening is achieved by merging 8 smaller blocks into a larger one. The BATSRUS code achieves excellent scaling on distributed memory parallel super-computers both with explicit
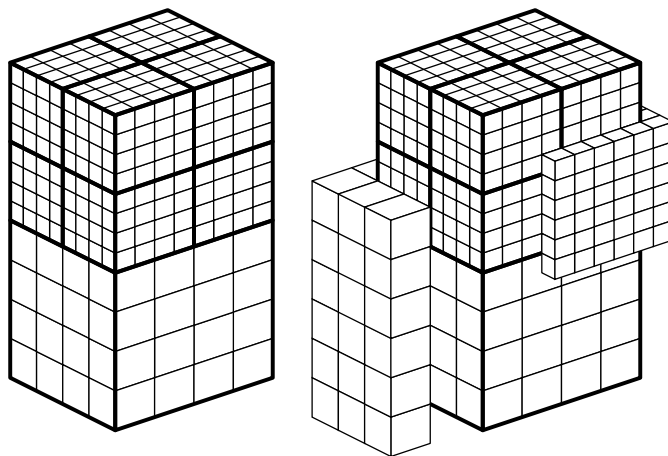

Fig. 1. The block-adaptive grid structure. Blocks are refined into 8 octants (left panel). The blocks communicate via layers of ghost cells (right panel).

and with implicit time-stepping. The implicit scheme is based on the Jacobian-free Newton–Krylov–Schwarz (NKS) method and it can be efficiently combined with the explicit scheme on a block-by-block basis [21].

Our goal is to add the new Hall MHD capability into BATSRUS while preserving compatibility with all the essential features: shock-capturing, high resolution second order TVD schemes, efficient explicit and implicit time stepping, block-adaptive grid for both Cartesian and non-Cartesian geometries, and good parallel scaling on distributed memory computers. We also allow for solving the Hall MHD in a limited region by introducing a spatially varying coefficient for the Hall term.

Section 2 presents the Hall MHD equations in conservation form and we discuss the analytic properties that are important for the discretization. In Section 3, we describe the second order discretization. Simple numerical tests as well as some typical geophysics applications are presented in Section 4. The tests demonstrate the second order accuracy of the scheme and the efficiency of the implicit time stepping scheme. We also demonstrate good parallel scaling up to more than thousand processors. We conclude in Section 5.

2. Equations

In Hall MHD the electric field is modified from the resistive MHD expression

$$\mathbf{E} = -\mathbf{v} \times \mathbf{B} + \eta \mathbf{J} \tag{1}$$

to the Hall MHD form

$$\mathbf{E} = -\mathbf{v} \times \mathbf{B} + \eta \mathbf{J} + \frac{1}{ne} \mathbf{J} \times \mathbf{B}, \tag{2}$$

where $\mathbf{v}$, $\mathbf{B}$, and $\mathbf{J}$ are the velocity, magnetic field and current vectors, respectively, η is the resistivity, n is the number density and e is the electron charge. Note that the magnetic units are chosen such that the magnetic permeability of vacuum μ_0 is unity. For sake of simplicity we neglect the electron pressure gradient term $\nabla p_e / (ne)$, although it can be discretized the same way as the Hall term $\mathbf{J} \times \mathbf{B} / (ne)$. The electron inertia is also neglected.

The electric field enters the induction and energy equations thus the MHD equations including the Hall term become

$$\frac{\partial \rho}{\partial t} = -\nabla \cdot (\rho \mathbf{v}), \tag{3}$$

$$\frac{\partial \rho \mathbf{v}}{\partial t} = -\nabla \cdot \left(\mathbf{v} \rho \mathbf{v} + \bar{I} p + \bar{I} \frac{\mathbf{B}^2}{2} - \mathbf{B} \mathbf{B} \right), \tag{4}$$

$$\frac{\partial e}{\partial t} = -\nabla \cdot [\mathbf{v}(\varepsilon + p) + (\mathbf{v} + \mathbf{v}_H) \cdot (\bar{I} \mathbf{B}^2 - \mathbf{B} \mathbf{B}) - \mathbf{B} \times \eta \mathbf{J}], \tag{5}$$

$$\frac{\partial \mathbf{B}}{\partial t} = -\nabla \times [-(\mathbf{v} + \mathbf{v}_H) \times \mathbf{B} + \eta \mathbf{J}], \tag{6}$$

where $\bar{I}$ is the identity matrix, ρ and p are the mass density and the thermal pressure. The Hall velocity is defined as

$$v_H = -\frac{\mathbf{J}}{ne} = -\frac{\nabla \times \mathbf{B}}{ne}, \tag{7}$$

while the total energy density is

$$e = \varepsilon + \frac{\mathbf{B}^2}{2} = \frac{p}{\gamma - 1} + \frac{\rho \mathbf{v}^2}{2} + \frac{\mathbf{B}^2}{2}, \tag{8}$$

where ε is the hydrodynamic energy and γ is the adiabatic index.

For space physics simulations it is often useful to split the magnetic field into an analytic part and a numerical part $\mathbf{B} = \mathbf{B}_0 + \mathbf{B}_1$ [20]. The analytic $\mathbf{B}_0$ is a divergence and curl free potential field (e.g. the dipole field of a planet), while $\mathbf{B}_1$ contains the rest of the field. We allow $\mathbf{B}_0$ to be time dependent. The advantage of this split-

ting is that the numerical solution is more accurate and robust where gradients of $\mathbf{B}_0$ are large. Also one can introduce a reduced total energy density

$$e_1 = \varepsilon + \frac{\mathbf{B}_1^2}{2}, \tag{9}$$

that does not contain $\mathbf{B}_0$ or $\mathbf{B}_0^2$ which allows much more accurate and robust results in regions where $\mathbf{B}_0$ is large. The splitting results in the following energy and induction equations:

$$\frac{\partial e_1}{\partial t} = -\nabla \cdot [\mathbf{v}(\varepsilon + p) + (\mathbf{v} + \mathbf{v}_H) \cdot (\bar{I}\mathbf{B}_1^2 - \mathbf{B}_1\mathbf{B}) + \mathbf{v}_H \mathbf{B}_0 \cdot \mathbf{B}_1 - \mathbf{B} \times \eta\mathbf{J}] - \mathbf{B}_1 \cdot \frac{\partial \mathbf{B}_0}{\partial t}, \tag{10}$$

$$\frac{\partial \mathbf{B}_1}{\partial t} = -\nabla \times [-(\mathbf{v} + \mathbf{v}_H) \times \mathbf{B} + \eta\mathbf{J}] - \frac{\partial \mathbf{B}_0}{\partial t}. \tag{11}$$

There are only a few extra terms relative to classical MHD in the induction and energy density equations all proportional to v_H. This seemingly small modification of the MHD equations is quite challenging to implement in a conservative, accurate and efficient manner. There are two challenges:

- There is a second order spatial derivative of the magnetic field in the induction equation that cannot be rewritten into a simple Laplace operator.
- The maximum wave speed increases from the fast magnetosonic wave to the whistler wave speed that is approximately inversely proportional to the wave length.

The first problem is especially difficult because of the adaptive block structure of the BATSRUS code. It takes a lot of care to obtain a spatially second order accurate discretization at resolution changes. The second problem is important, because the shortest wave length that can be represented on the grid is twice the grid resolution Δx, so the fastest wave speed can be estimated as [8]

$$c_w = |v| + c_f + \frac{|B|\pi}{en\Delta x}, \tag{12}$$

where c_f is the classical MHD fast magnetosonic speed. The maximum stable time step for an explicit time integration scheme is

$$\Delta t < \frac{\Delta x}{c_w} \propto \Delta x^2 \tag{13}$$

for small enough Δx. This can make the explicit time integration algorithms rather inefficient as the grid resolution is increased. An implicit scheme can potentially overcome this problem, since the time step is not limited by the CFL condition.

An additional difficulty arises, since the numerical dissipation required for the stability of the explicit numerical scheme is also proportional to the fastest wave speed of the hyperbolic system of equations, and this can reduce the spatial order of accuracy by one order. To see this, let us consider the *usually* first order accurate local Lax–Friedrichs scheme

$$\frac{U^{n+1} - U^n}{\Delta t} = -\frac{F_{i+1}^n - F_{i-1}^n}{2\Delta x} + \frac{c_{i+1/2}(U_{i+1}^n - U_i^n) - c_{i-1/2}(U_i^n - U_{i-1}^n)}{2\Delta x}, \tag{14}$$

where U is one of the conservative variables, F is the corresponding physical flux function, and c is the fastest wave speed. The superscripts denote the time level and the subscripts correspond to the spatial grid indexes. The index $i + 1/2$ identifies the cell face between the cell centers i and $i + 1$. The second term on the right hand side is the numerical dissipation and to lowest order in Δx it is proportional to

$$\Delta x \frac{\partial}{\partial x}\left(c\frac{\partial U}{\partial x}\right). \tag{15}$$

Since $c \propto 1/\Delta x$ the local Lax–Friedrichs scheme is **inconsistent** for the Hall MHD equation.

In the following section we will describe our solutions to these challenging problems.

3. Numerical discretization

3.1. Spatial discretization of the current for uniform grid

A second order conservative scheme requires a second order accurate calculation of the physical fluxes at the center of the cell faces. Since the flux for the magnetic field **B** contains the Hall term $\mathbf{J} \times \mathbf{B}/ne$ and $\mathbf{J} = \nabla \times \mathbf{B}$, we have to calculate the current with second order accuracy at the cell faces. For the x face of a uniform Cartesian grid one can use simple central differencing and averaging as needed:

$$J^x_{i+1/2,j,k} = \frac{B^z_{i,j+1,k} + B^z_{i+1,j+1,k} - B^z_{i,j-1,k} - B^z_{i+1,j-1,k}}{4\Delta y} - \frac{B^y_{i,j,k+1} + B^y_{i+1,j,k+1} - B^y_{i,j,k-1} - B^y_{i+1,j,k-1}}{4\Delta z}$$

$$J^y_{i+1/2,j,k} = \frac{B^x_{i,j,k+1} + B^x_{i+1,j,k+1} - B^x_{i,j,k-1} - B^x_{i+1,j,k-1}}{4\Delta z} - \frac{B^z_{i+1,j,k} - B^z_{i,j,k}}{\Delta x} \qquad (16)$$

$$J^z_{i+1/2,j,k} = \frac{B^y_{i+1,j,k} - B^y_{i,j,k}}{\Delta x} - \frac{B^x_{i,j+1,k} + B^x_{i+1,j+1,k} - B^x_{i,j-1,k} - B^x_{i+1,j-1,k}}{4\Delta y}$$

and similar formulas apply to the other faces. Note that the normal derivatives use the two closest cell centers only, while the tangential derivatives require 4 cell centers and averaging in the i direction. Consequently one needs to use the first layer of ghost cells not only at the faces between the blocks but also along the 12 edges of the block. Fig. 2 shows the stencil used for calculating the three components of the current at the x face center on a two-dimensional grid.

3.2. Spatial discretization of the current at resolution changes

The second order accurate central difference formulas (16) used to calculate the curl of **B** on a uniform grid can be used at resolution changes as well if the ghost cells are filled in with at least third order accurate magnetic field. An alternative is to use a one sided derivative. For example the y gradient of B^z at the cell center j can be approximated as

$$\left(\frac{\partial B^z}{\partial y}\right)_j = \frac{-3B^z_j + 4B^z_{j+1} - B^z_{j+2}}{2\Delta y}. \qquad (17)$$

We use this latter approach to avoid the use of ghost cells in the tangential (relative to the face) derivatives on the coarse side of resolution changes. On the fine side we take the first approach, ie. interpolate the magnetic field to the fine ghost cells with third order accuracy. This is not a unique choice, there are many other possible discretizations.

3.3. Spatial discretization of the magnetic field at resolution changes

Let us consider a face orthogonal to the x direction indexed by $1/2$, j, k and assume that the ghost cells 0, j, k cover the domain of a coarser block. We are interested in calculating the current for the fine block because the flux on the coarse side is overwritten by the sum of the 4 fine fluxes [1] in a conservative AMR scheme. The interpolation of the magnetic field has to be third order accurate so that the derived current can be second
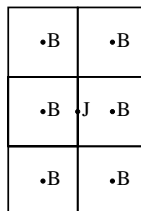

Fig. 2. The stencil for calculating the face centered current on a two-dimensional grid.

order accurate. Third order accuracy is quite complicated to achieve in finite volume discretization, so we take a finite difference approach and regard the cell center values to be point values (and not cell averages).

The first step is to interpolate the coarse cell values in the tangential direction to the y_j, z_k coordinates. For example the $j = k = 1$ index is interpolated from 3 coarse cell values covering the fine ghost cells $j, k \in \{-1, 0\}$, $j, k \in \{1, 2\}$ and $j, k \in \{3, 4\}$. In general when both j and k are odd numbers the interpolation formula is

$$\mathbf{B}_{-1/2,j,k} = \frac{5\mathbf{B}_{-1/2,j-3/2,k-3/2} + 30\mathbf{B}_{-1/2,j+1/2,k+1/2} - 3\mathbf{B}_{-1/2,j+5/2,k+5/2}}{32}. \tag{18}$$

Note that the 3 coarse cells are collinear with the fine cell along a diagonal line in the y, z plane. Cells with even j and k or even and odd j and k use a different set of coarse cells but the weights are the same. Next the fine cells inside the fine block and the interpolated coarse cell value are interpolated in the x direction along the j, k grid lines

$$\mathbf{B}_{0,j,k} = \frac{8\mathbf{B}_{-1/2,j,k} + 10\mathbf{B}_{1,j,k} - 3\mathbf{B}_{2,j,k}}{15}. \tag{19}$$

The same interpolation scheme is used for the other 5 faces. Fig. 3 shows the interpolation weights for the two-dimensional case.

The edge ghost cells are filled in with a similar approach. For example the edge ghost cells indexed by 0, 0, k are interpolated from 2 fine cells inside the fine block and the coarse cell values interpolated in the z direction

$$\mathbf{B}_{0,0,k} = \frac{8\mathbf{B}_{-1/2,-1/2,k} + 10\mathbf{B}_{1,1,k} - 3\mathbf{B}_{2,2,k}}{15}, \tag{20}$$

where

$$\mathbf{B}_{-1/2,-1/2,k} = \frac{5\mathbf{B}_{-1/2,-1/2,k-3/2} + 30\mathbf{B}_{-1/2,-1/2,k+1/2} - 3\mathbf{B}_{-1/2,-1/2,k+5/2}}{32} \tag{21}$$

for odd values of k and

$$\mathbf{B}_{-1/2,-1/2,k} = \frac{5\mathbf{B}_{-1/2,-1/2,k+3/2} + 30\mathbf{B}_{-1/2,-1/2,k-1/2} - 3\mathbf{B}_{-1/2,-1/2,k-5/2}}{32} \tag{22}$$

for even values of k. The edges parallel with the x and y axes are filled in similarly.

3.4. Discretization of the current for non-Cartesian geometries

We use the generalized coordinate approach to calculate the current with second order accuracy on non-Cartesian grids. The formulas developed in the previous subsections for taking gradients in the x, y and z
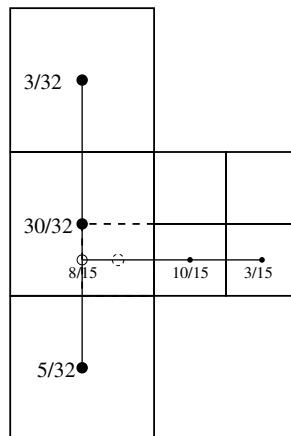

Fig. 3. The weights used to interpolate the magnetic field to the fine ghost cell (dashed circle) with 3rd order accuracy on a two-dimensional grid. First the coarse ghost cell centers (large dots) are interpolated in the vertical direction, next the interpolated value (circle) and the fine cell centers (small dots) are interpolated in the horizontal direction.

directions can be used without any change to obtain second order accurate derivatives of the magnetic field components B^x, B^y and B^z with respect to the generalized coordinates ξ, η, ζ. From these one can obtain the x, y and z derivatives using the coordinate transformation matrix $T = \partial(\xi, \eta, \zeta)/\partial(x, y, z)$, for example

$$\frac{\partial B^z}{\partial y} = \frac{\partial \xi}{\partial y}\frac{\partial B^z}{\partial \xi} + \frac{\partial \eta}{\partial y}\frac{\partial B^z}{\partial \eta} + \frac{\partial \zeta}{\partial y}\frac{\partial B^z}{\partial \zeta}. \tag{23}$$

The elements of matrix T can either be calculated analytically, or they can be obtained numerically by discretizing and inverting $T^{-1} = \partial(x, y, z)/\partial(\xi, \eta, \zeta)$. Elements of T^{-1} at the face $i + 1/2, j, k$ are obtained with the following fourth order accurate formulas:

$$\left(\frac{\partial \mathbf{x}}{\partial \xi}\right)_{i+1/2,j,k} = \frac{27(\mathbf{x}_{i+1,j,k} - \mathbf{x}_{i,j,k}) - (\mathbf{x}_{i+2,j,k} - \mathbf{x}_{i-1,j,k})}{24\Delta\xi},$$

$$\left(\frac{\partial \mathbf{x}}{\partial \eta}\right)_{i+1/2,j,k} = \frac{9\left(\frac{\partial \mathbf{x}}{\partial \eta}\right)_{i,j,k} + 9\left(\frac{\partial \mathbf{x}}{\partial \eta}\right)_{i+1,j,k} - \left(\frac{\partial \mathbf{x}}{\partial \eta}\right)_{i-1,j,k} - \left(\frac{\partial \mathbf{x}}{\partial \eta}\right)_{i+2,j,k}}{16}, \tag{24}$$

$$\left(\frac{\partial \mathbf{x}}{\partial \zeta}\right)_{i+1/2,j,k} = \frac{9\left(\frac{\partial \mathbf{x}}{\partial \zeta}\right)_{i,j,k} + 9\left(\frac{\partial \mathbf{x}}{\partial \zeta}\right)_{i+1,j,k} - \left(\frac{\partial \mathbf{x}}{\partial \zeta}\right)_{i-1,j,k} - \left(\frac{\partial \mathbf{x}}{\partial \zeta}\right)_{i+2,j,k}}{16},$$

where the transverse gradients are obtained as

$$\left(\frac{\partial \mathbf{x}}{\partial \eta}\right)_{i,j,k} = \frac{8(\mathbf{x}_{i,j+1,k} - \mathbf{x}_{i,j-1,k}) - (\mathbf{x}_{i,j+2,k} - \mathbf{x}_{i,j-2,k})}{12\Delta\eta}, \tag{25}$$

$$\left(\frac{\partial \mathbf{x}}{\partial \zeta}\right)_{i,j,k} = \frac{8(\mathbf{x}_{i,j,k+1} - \mathbf{x}_{i,j,k-1}) - (\mathbf{x}_{i,j,k+2} - \mathbf{x}_{i,j,k-2})}{12\Delta\zeta}. \tag{26}$$

Here we can safely use the ghost cells, since the coordinates of the ghost cell centers are exact. The formulas for the y and z faces can be derived in an analogous fashion.

3.5. Second order explicit scheme

The main challenge for the explicit time integration scheme is to preserve the stability without losing the order of accuracy. In the previous subsections we showed how the current can be discretized at the cell interfaces. Using this current it is straightforward to construct the second order accurate physical flux. The remaining task is to use a numerical dissipation that is stable and second order accurate. As we have shown the naive implementation of the first order Lax–Friedrichs scheme (14) is inconsistent for the Hall MHD equations.

We use the MUSCL approach [22] to get a consistent and second order accurate TVD scheme. The state variable U is extrapolated from the left and right cell centers to the cell face at $i + 1/2$ as

$$U^L_{i+1/2} = U_i + \frac{1}{2}\overline{\Delta}U_i,$$

$$U^R_{i+1/2} = U_{i+1} - \frac{1}{2}\overline{\Delta}U_{i+1}, \tag{27}$$

where $\overline{\Delta}U_i$ is the limited slope in cell i. The divergence of the numerical flux (the last term in 14) is modified to

$$\Phi_i = \frac{c_{i+1/2}(U^R_{i+1/2} - U^L_{i+1/2}) - c_{i-1/2}(U^R_{i-1/2} - U^L_{i-1/2})}{2\Delta x}. \tag{28}$$

In classical MHD c does not depend on Δx and the numerical dissipation is a second order term as long as the limited slopes are consistent, i.e. $\overline{\Delta}U_i \to (U_{i+1} - U_i)$ when $(U_{i+1} - U_i) \to (U_i - U_{i-1})$. For Hall MHD we need higher order accuracy, and it turns out that only a certain class of limiters can be used. The simplest, most robust and quite commonly used minmod limiter is defined as

$$\overline{\Delta}U_i = \text{minmod}(U_{i+1} - U_i, U_i - U_{i-1}), \tag{29}$$

where the minmod function returns 0 if the arguments have different signs, otherwise it returns the argument with the smallest magnitude. The minmod limiter is asymmetric in the sense that it either takes the left slope or the right slope, depending on the second derivative of the solution. Due to the asymmetry the numerical flux in (28) is proportional to $c\Delta x^2 \partial^3 U / \partial x^3$ (here we take c to be constant for simplicity) so the scheme is first order accurate only in general.

On the other hand the monotonized central limiter

$$\overline{\Delta} U_i = \text{minmod}\left[\beta(U_{i+1} - U_i), \beta(U_i - U_{i-1}), \frac{U_{i+1} - U_{i-1}}{2}\right] \tag{30}$$

with $1 < \beta \leqslant 2$ is symmetric as long as the last argument, (the central difference) has the smallest magnitude. This is true in sufficiently smooth parts of the solution and away from local extrema. Substituting the central difference into equations (27) and then into (28) we get

$$\Phi = \frac{c_{i+1/2}\left(U_{i+1} - \frac{U_{i+2} - U_i}{4} - U_i - \frac{U_{i+1} - U_{i-1}}{4}\right)}{2\Delta x} - \frac{c_{i-1/2}\left(U_i - \frac{U_{i+1} - U_{i-1}}{4} - U_{i-1} - \frac{U_i - U_{i-2}}{4}\right)}{2\Delta x}. \tag{31}$$

For sufficiently smooth solutions this can be rewritten up to the lowest order non-zero terms in Δx as

$$\Phi_i = -\frac{(c_{i+1/2} + c_{i-1/2})\frac{\partial^4 U}{\partial x^4}\Big|_i \Delta x^4 + (c_{i+1/2} - c_{i-1/2})\frac{\partial^3 U}{\partial x^3}\Big|_i \Delta x^3}{16\Delta x}. \tag{32}$$

Since according to (12) $c \propto 1/\Delta x$ the first term on the right hand side is proportional to Δx^2. The second term contains the difference $(c_{i+1/2} - c_{i-1/2})$ that can be approximated as $(\partial c/\partial U) \cdot (\partial U/\partial x)_i \Delta x \propto O(1)$, so the second term is also proportional to Δx^2. This proves that the use of a symmetric limiter achieves the required second order accuracy.

We note that for ordinary MHD (or any hyperbolic system where the wave speed does not depend on the wave length) the MC limiter has a third order dissipation in smooth regions as opposed to the asymmetric minmod (or superbee) limiters that have second order dissipation at best. One can also construct limiters with different weights in the left and right extrapolations that give third order accuracy for the physical fluxes as well. Using

$$\overline{\Delta}^L U_i = \text{minmod}\left[\beta(U_{i+1} - U_i), \beta(U_i - U_{i-1}), \frac{2U_{i+1} - U_i - U_{i-1}}{3}\right] \tag{33}$$

$$\overline{\Delta}^R U_i = \text{minmod}\left[\beta(U_{i+1} - U_i), \beta(U_i - U_{i-1}), \frac{U_{i+1} - U_i - 2U_{i-1}}{3}\right] \tag{34}$$

for the left and right extrapolations in (27), respectively, results in a third order accurate scheme in sufficiently smooth regions away from local extrema. This is the same as Koren's limiter [9] but with an adjustable β parameter.

Finally, we point out the similarity between the dissipation terms arising from the symmetric limiter and the fourth (or higher) order hyper-resistivity used in several Hall MHD codes (e.g. [3,25,24]). If we substitute the dominant term of c_w in (12) into the first term of (32) we obtain the numerical dissipation

$$\Phi_i = -\frac{|B|\pi}{8en}\frac{\partial^4 U}{\partial x^4}\Big|_i \Delta x^2. \tag{35}$$

This is essentially the same form as the fourth order hyper-resistivity often used to stabilize the induction equation. Note, however, that the TVD scheme switches to lower order dissipation where the solution is not smooth, while the hyper-resistivity is applied uniformly everywhere. Another difference is that the TVD scheme is applied to all of the Hall MHD equations, while the hyper-resistivity is only applied to the induction equation, and the other equations are usually stabilized in a different manner.

We also note that the explicit Hall Diffusion Scheme (HDS) described by Sullivan and Downes [15] also results in a fourth order hyper-resistivity term once the update equations for the B_y and B_z components (equations 29 and 30 in their paper) are substituted into each other. The HDS scheme is essentially a two stage formulation of the one stage hyper-resistivity scheme.

3.6. Implicit time discretization

We use the Newton–Krylov–Schwarz (NKS) approach to formulate the implicit time integration scheme for Hall MHD. Thanks to the general implementation of the implicit scheme in the BATSRUS code [21], once the explicit Hall MHD scheme is implemented, the implicit time integration works as well. To make it efficient, however, the preconditioner needs to take into account the Hall term. This is not a simple task. For sake of simplicity and efficiency the preconditioner is based on the Jacobian that uses the nearest 6 neighbor cells only on a three-dimensional grid. Due to the higher order derivatives, the stencil of the Hall term is much more extended. We found that the preconditioner becomes much more effective if the Hall term is discretized on a stencil that is as compact as possible. In particular, when the current is calculated for the X face at $i + 1/2, j, k$, all x derivatives should use only the $i + 1$ and i cell centers only.

An additional difficulty arises due to the particular choice of the implicit scheme. For sake of efficiency a spatially first order local Lax–Friedrichs (or HLL or Roe) discretization is used in the matrix-free calculation of the Jacobian. The corresponding error term is $c\Delta x\Delta t$ which is second order for classical MHD, but it is only first order accurate for Hall MHD, since $c \propto 1/\Delta x$ and for the implicit scheme the time step is decreased as $\Delta t \propto \Delta x$ as the resolution is increased.

To resolve this problem, we exploit that for the implicit time step it is not necessary to include the full whistler wave speed into the numerical flux function. In fact, our numerical tests confirmed that it leads to significant degradation of accuracy, if we use the full speed $c = c_w$ in the numerical flux. Since the stability of the implicit scheme does not depend on the numerical dissipation, one can use a reduced speed

$$c = |u| + c_f + W\frac{\pi|B|}{\Delta xen}, \tag{36}$$

where $W < 1$. According to Chacon and Knoll [4] a good choice is $W \propto \Delta t_{\text{expl}}/\Delta t$, where Δt_{expl} is the time step for the explicit scheme. This way $W \propto \Delta x$, the c used in the numerical flux becomes independent of the resolution, and the second order accuracy is recovered. An even simpler choice is to set $W = 0$ that seems to work fine in our experience.

3.7. Preconditioner

The general preconditioner described in [21] (and implemented in BATSRUS) calculates the Jacobian with the assumption that the face flux in the Lax–Friedrichs scheme is

$$\mathbf{F}_{i+1/2,j,k} = \frac{\mathbf{F}_{i,j,k} + \mathbf{F}_{i+1,j,k}}{2} \tag{37}$$

and $\mathbf{F}_{i,j,k}$ is a function of the local state variable $\mathbf{U}_{i,j,k}$ only. The Hall term in the cell centered flux function used by this preconditioner is

$$\mathbf{F}_{\text{H}}(\mathbf{B})_{i,j,k} = (\mathbf{v}_H\mathbf{B} - \mathbf{B}\mathbf{v}_H)_{i,j,k} = -\left(\frac{\mathbf{JB} - \mathbf{BJ}}{ne}\right)_{i,j,k}, \tag{38}$$

where the current $\mathbf{J}_{i,j,k}$ is evaluated with a cell centered approximation. As we take the partial derivatives $\partial\mathbf{F}_{i,j,k}/\partial\mathbf{U}_{i,j,k}$, the current $\mathbf{J}_{i,j,k}$ will behave as a constant multiplier, since it depends on the magnetic field in the neighbor cells only. Unfortunately this neglects the most important terms that are responsible for the whistler wave, and make the preconditioner useless for a Hall term dominated problem. To obtain an efficient preconditioner, we need to add the partial derivatives that are not included by the general preconditioner algorithm.

The face flux of the magnetic field contains the current $\mathbf{J}_{i+1/2,j,k}$ that is discretized by (16) and depends on the cell values $\mathbf{B}_{i,j,k}, \mathbf{B}_{i,j\pm1,k}, \mathbf{B}_{i,j,k\pm1}$, $\mathbf{B}_{i+1,j,k}, \mathbf{B}_{i+1,j\pm1,k}$, and $\mathbf{B}_{i+1,j,k\pm1}$. For sake of computational efficiency, the preconditioner is limited to the adjacent cells $(i \pm 1, j, k)$, $(i, j \pm 1, k)$, and $(i, j, k \pm 1)$ so that the approximate Jacobian is restricted to a block heptadiagonal matrix. This means that we drop all fractions in (16) that have four terms in the numerator. The remaining two fractions describe the orthogonal (with respect to the face) derivatives of the tangential components of the magnetic field. Substituting these current terms into the discretized induction equation results in

$$R_H(B_{i,j,k}^y) = -\Delta x^{-2}\left[\left(\frac{B^x}{ne}\right)_{i+1/2,j,k}(B_{i+1,j,k}^z - B_{i,j,k}^z) + \left(\frac{B^x}{ne}\right)_{i-1/2,j,k}(B_{i-1,j,k}^z - B_{i,j,k}^z)\right] \tag{39}$$

$$R_H(B_{i,j,k}^z) = +\Delta x^{-2}\left[\left(\frac{B^x}{ne}\right)_{i+1/2,j,k}(B_{i+1,j,k}^y - B_{i,j,k}^y) + \left(\frac{B^x}{ne}\right)_{i-1/2,j,k}(B_{i-1,j,k}^y - B_{i,j,k}^y)\right] \tag{40}$$

and similar terms for the y and z faces. Here $R_H = -\nabla \cdot F_H$ is the change of $\mathbf{B}$ due to the Hall term. The partial derivatives of the $B^x/(ne)$ terms are properly approximated by the general algorithm that calculates $[(\partial \mathbf{F}/\partial \mathbf{U})_{i+1} - (\partial \mathbf{F}/\partial \mathbf{U})_{i-1}]/(2\Delta x)$. The extra terms that correspond to the partial derivatives of the current with respect to the magnetic field, are obtained analytically and added to the Jacobian matrix, e.g.

$$\frac{\partial R_H(B_{i,j,k}^y)}{\partial B_{i+1,j,k}^z} = -\Delta x^{-2}\left(\frac{B^x}{ne}\right)_{i+1/2,j,k}. \tag{41}$$

Although we dropped a lot of terms from (16), the preconditioner still contains the essential terms that are responsible for the whistler waves. To see this, let us take the case when the ambient magnetic field is homogeneous and aligned with the x axis, the velocity is zero, and the density is also homogeneous. Then (39) is a discretization of

$$\frac{\partial B^y}{\partial t} = -\frac{B^x}{ne}\frac{\partial^2 B^z}{\partial x^2} \tag{42}$$

$$\frac{\partial B^z}{\partial t} = +\frac{B^x}{ne}\frac{\partial^2 B^y}{\partial x^2} \tag{43}$$

that can be combined to

$$\frac{\partial^2 B^y}{\partial t^2} = -\left(\frac{B^x}{ne}\right)^2\frac{\partial^4 B^y}{\partial x^4}. \tag{44}$$

Substituting $B_y = \exp i(kx - \omega t)$ gives the dispersion relation

$$\omega^2 = \left(\frac{B^x}{ne}\right)^2 k^4 \tag{45}$$

and the wave speed for a fixed wave number is

$$c = \frac{\omega}{k} = \frac{k|B^x|}{ne} = \frac{2\pi B}{\lambda ne} \tag{46}$$

that is the whistler wave speed. Substituting $\lambda = 2\Delta x$ results in the last and dominant term of (12).

3.8. Preconditioner for generalized coordinates

To derive the preconditioner in generalized coordinates, we start from the discrete form of the induction equation for a particular grid cell and we deal with the contribution of the Hall term only:

$$R_H(\mathbf{B}) = \frac{1}{V}\sum_s \frac{\mathbf{A}^s}{n^s e} \cdot (\mathbf{B}^s\mathbf{J}^s - \mathbf{J}^s\mathbf{B}^s), \tag{47}$$

where V is the cell volume, s indexes the faces of the cell, and $\mathbf{A}^s$ is the outward pointing area vector for face s. The current $\mathbf{J}^s$ is discretized with partial derivatives with respect to the generalized coordinates multiplied by the coordinate transformation matrix $T = \partial \xi/\partial \mathbf{x}$ as in (23). For component B_j the above equation becomes

$$R_H(B_j) = \frac{1}{V}\sum_s \frac{A_i^s}{n^s e}(B_i^s \epsilon_{jkl} - B_j^s \epsilon_{ikl})T_{k\alpha}^s \partial_\alpha B_l^s, \tag{48}$$

where ϵ is the Levi–Civita tensor and summation is implied for repeated indexes. The i, j, k, l indexes are for the Cartesian coordinates x, y, z, while the α index is for the generalized coordinates ξ, η, ζ.

Just like in the Cartesian case, the partial derivatives of R_H with respect to B_i^s and B_j^s are properly taken into account by the general algorithm. We only need to calculate the extra terms that correspond to the derivatives of B_l. Since we constrain the preconditioner matrix to the neighboring cells, only the discrete difference along the direction $\alpha = \sigma$ normal to face s is kept when taking the derivatives:

$$\partial_\sigma B_l^s = \pm \frac{B_l^S - B_l}{\Delta \sigma}, \tag{49}$$

where B_l^s is the magnetic field at the center of the neighbor cell on the other side of face s. The plus sign is taken for the face pointing toward the positive σ direction. Now we are ready to calculate the extra elements of the $\partial \mathbf{R}_H / \partial \mathbf{B}$ matrix needed for the preconditioner:

$$\frac{\partial R_H(B_j)}{B_l} = \frac{1}{V} \sum_s \frac{\mp A_i^s}{n^s e} \left(B_i^s \epsilon_{jkl} - B_j^s \epsilon_{ikl} \right) \frac{T_{k\sigma}^s}{\Delta \sigma}, \tag{50}$$

$$\frac{\partial R_H(B_j)}{B_l^S} = \pm \frac{A_i^s}{V n^s e} \left(B_i^s \epsilon_{jkl} - B_j^s \epsilon_{ikl} \right) \frac{T_{k\sigma}^s}{\Delta \sigma}. \tag{51}$$

One may further simplify the preconditioner by taking the cell center values n, B_i, B_j and $T_{k\sigma}$ instead of the face centered values n^s, B_i^s, B_j^s and $T_{k\sigma}^s$, respectively. For sake of computational efficiency we have implemented this simplified form.

As a consistency check we show that the preconditioner developed for the generalized coordinates simplifies to the Cartesian preconditioner for Cartesian coordinates, when $T_{k\sigma}/\Delta \sigma = \delta_{k\sigma}/\Delta x_k$ and $A_i^s/V = \pm \delta_{is}/\Delta x_s$. Here δ denotes the Kronecker delta and $\sigma = s = k = i$. With these the above formulas simplify to

$$\frac{\partial R_H(B_j)}{B_l} = \sum_s \frac{B_s^s \epsilon_{sjl}}{\Delta x_s^2 n^s e}, \tag{52}$$

$$\frac{\partial R_H(B_j)}{B_l^S} = - \frac{B_s^s \epsilon_{sjl}}{\Delta x_s^2 n^s e}. \tag{53}$$

This is the Cartesian preconditioner written in a general notation. For example, for $s = x$, $j = y$, $l = z$ and $S = i + 1$ the last equation coincides with (41).

4. Numerical tests

4.1. Propagation of the whistler wave

To verify the accuracy of the algorithm and the correctness of the implementation, we simulate the propagation of the whistler wave in a periodic box. In our standard runs we use the second order MUSCL scheme with the Lax–Friedrichs flux and the MC limiter with $\beta = 1.5$. The explicit runs use a two stage Runge–Kutta scheme with a CFL number 0.8. The implicit runs use the BDF2 scheme, a time step linearly proportional to the cell size, and a reduced numerical flux with $W = 0$ in (36). We apply the 8-wave scheme to control the divergence of the magnetic field in the two-dimensional test, although this is not really necessary in these test runs. Any deviation from these standard parameters will be noted.

We start with the grid aligned case on a uniform grid. The computational domain is $-100 < x < 100$ with periodic boundaries. The initial condition is uniform for the following variables: $\rho = 1$, $v_x = -0.001$, $B_x = 100$ and $P = 1$, so the Alfvén speed is $c_A = B_x / \sqrt{\rho} = 100$ and the sound speed is $c_S = \sqrt{\gamma p / \rho} \approx 1.291$ where $\gamma = 5/3$. The choice of a non-zero v_x avoids the problems with normalization in the implicit scheme. To make the whistler wave speed comparable to the Alfvén speed, we set the ion mass per charge $M/e = 35.1076$ (an admittedly arbitrary number in the normalized units). We will study the longest wave that fits into the computational domain, so the wave length is $\lambda = 200$ and the wave number is $k = 2\pi/\lambda = \pi/100$. The exact formula for the phase speed of the right going whistler wave relative to the fluid is

$$c_w = \frac{\omega}{k} = \frac{w}{2} + \sqrt{c_A^2 + \frac{w^2}{4}} \approx 169.345, \tag{54}$$

where $w = (M/e)(k|B|)/\rho \approx 110.294$, and the amplitude ratio of the transverse velocity and magnetic perturbations is

$$\frac{|\delta v_{y,z}|}{|\delta B_{y,z}|} = \frac{|B_x|}{c_w \rho} \approx 0.59051. \tag{55}$$

The whistler wave is initialized with

$$v_y = -0.00590511 \cos(kx), \tag{56}$$
$$v_z = +0.00590511 \sin(kx), \tag{57}$$
$$B_y = +0.001 \cos(kx), \tag{58}$$
$$B_z = -0.001 \sin(kx). \tag{59}$$

Note that this is a circularly polarized wave, and the velocity (and the electric field) is right-hand circularly polarized. The pressure, the density and the x components of the velocity and magnetic field are not affected by the wave. The final time is set to $t_{\max} = \lambda/|u_x + c_w| \approx 1.18103$ so that the wave arrives back at the original position by the end of the run. The numerical error is calculated from the difference between the initial and final v_z:

$$E_n = \frac{\sum_{i=1}^{n} |v_{z,i}(t_{\max}) - v_{z,i}(0)|}{\sum_{i=1}^{n} |v_{z,i}(0)|}, \tag{60}$$

where $i = 1, \ldots, n$ indexes the grid cells in the whole computational domain. We could use the error in v_y, B_y or B_z just as well, and the results would remain essentially the same.

We repeat the simulation with 4 different resolutions using $n = 16, 32, 64, 128$ cells, respectively. The explicit scheme requires 141, 489, 1811, and 6955 time steps respectively, ie. the time step Δt is roughly proportional to $1/\Delta x^2$. For the implicit scheme the time step is set to be proportional to $1/\Delta x$ and it takes 40, 80, 160 and 320 time steps to finish the runs, respectively. As expected, the implicit time stepping becomes relatively more efficient at finer resolutions.

The first four columns of Table 1 contain the errors of the explicit runs with minmod and MC limiters and the implicit runs with $W = 1$ and $W = 0$ in (36) both with the MC limiter, respectively. The fifth column is the implicit scheme with $W = 0$ and the minmod limiter. In accordance with the analysis presented in Subsection 3.5 the explicit scheme with the minmod limiter provides a roughly first order convergence rate only, while the MC limiter gives almost perfect second order convergence. Similarly, the implicit scheme using a numerical flux based on the full wave speed gives first order convergence rate only, while setting $W = 0$ in (36) provides second order convergence rate, in full agreement with the discussion in Section 3.6. The implicit scheme with $W = 0$ and the minmod limiter converges at a second order rate although the results are less accurate than for the MC limiter (columns 4 and 5). It is interesting to note that the implicit scheme is more accurate than the explicit scheme (compare columns 2 and 4). This is due to the fact that explicit scheme requires the full numerical flux with $W = 1$ for stability, while the implicit scheme is stable with a less diffusive numerical flux too.

We repeated the test on a two-dimensional uniform grid with rotated initial conditions. The rotation angle is $\alpha = \tan^{-1} 0.5 = 26.56°$ so there is a translational symmetry in the (1, 2) direction as shown in Fig. 4. The boundary conditions remain periodic in the X direction, while we apply a sheared zero gradient in the (1, 2) direction along the Y boundaries. The length of the computational domain is increased by a factor of $1/\cos(\alpha) = \sqrt{5}/2$ to $-111.803 < x < 111.803$ to maintain the periodicity in the X direction. All the vector

Table 1
Relative errors for whistler wave test on a uniform grid

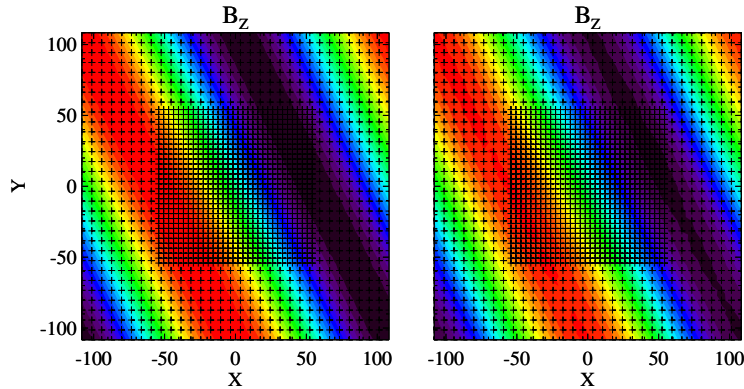| n	expl/mm	explicit	impl/$W = 1$	implicit	impl/mm	expl/rot	impl/rot
16	1.236	0.42261	0.875	0.15352	0.19424	0.30733	0.18311
32	0.614	0.08537	0.465	0.03856	0.04881	0.06167	0.04266
64	0.265	0.01926	0.243	0.00100	0.01234	0.01388	0.01034
128	0.118	0.00519	0.124	0.00277	0.00316	0.00373	0.00304

Fig. 4. The z component of the magnetic field at the initial (left panel) and final (right panel) times for the whistler wave test on a periodic non-uniform grid. The crosses indicate the cell centers.

Table 2
Relative errors for whistler wave test on a non-uniform grid

n	explicit	implicit	expl/rot.	impl/rot.
24	0.2514	0.05218	0.2632	0.07958
48	0.0517	0.01244	0.0522	0.01968
96	0.0114	0.00305	0.0124	0.00490

variables (velocity and magnetic field) as well as the perturbation are rotated by α. As the last two columns of Table 1 shows, the convergence rate remains second order. Somewhat surprisingly the errors for the rotated explicit run are somewhat smaller than in the grid aligned case. This is probably due to the fact that the numerical flux is proportional to $|B_x|$ and $|B_y|$, which is different in the rotated case than in the grid aligned case.

The next set of tests are done on a non-uniform grid. We refine the middle part of the grid for $|x| < 50$ in the 1D case, and $|x|, |y| < 50/\cos\alpha$ in the two-dimensional case. The error is calculated the same way as for the uniform grid (equal weight for all cells). The results are shown in Table 2 for the explicit and implicit schemes with grid-aligned and rotated initial conditions. The number of cells refer to a 1D cut, e.g. $n = 48$ corresponds to the base grid with $n = 32$ which is refined in the middle adding another 16 cells. The time step for the explicit scheme is determined by the smaller cells. For the implicit scheme we also used the same time step as on the uniform grid corresponding to the finer cells, so the number of explicit and implicit steps for $n = 24, 48, 96$ are 489, 1811, 6955 and 80, 160, 320, respectively. The results confirm that the scheme remains second order accurate at resolution changes.

4.2. Reconnection in the GEM challenge

The Geospace Environmental Modeling (GEM) magnetic reconnection challenge [3] is a very well studied two-dimensional reconnection problem. There are several published solutions obtained with other Hall MHD codes, so this problem is suitable to further verify our implementation.

The computational domain is $L_x = 25.6$ times $L_z = 12.8$ centered around the origin (for sake of comparison we follow [3] and use x and z coordinates). The initial condition is

$$B_x = \tanh(2z) - A_y(\pi/L_z)\cos(2\pi x/L_x)\sin(\pi z/L_z) \tag{61}$$

$$B_z = A_y(2\pi/L_x)\cos(2\pi x/L_x)\sin(\pi z/L_z) \tag{62}$$

$$p = 0.6 - \tanh(2z)^2/2 \tag{63}$$

with $\mathbf{v} = 0$, $B_y = 0$ and $\rho = 2p$ so that the normalized temperature is 1/2. The adiabatic index is $\gamma = 5/3$. The perturbation of the magnetic field is defined through the vector potential with amplitude A_y. Without this perturbation the current sheet is in pressure equilibrium. The boundary conditions are periodic in the x direc-

tion, and floating (zero gradient) for the other boundaries (instead of ideally conducting). The simulation is run until $t = 40$.

The initial perturbation forces the reconnection site to be at the origin. We found, however, that in the Hall MHD simulations the configuration evolves into two reconnection sites and an island in the middle (see Fig. 5), as long as the initial perturbation is small ($A_y = 0.1$). For larger initial perturbation ($A_y = 0.5$) the single reconnection site is stable. We note that the formation of an island in the GEM challenge problem is not unique to our code (J. Huba, L. Chacon private communications).

The computational domain is resolved by 64 times 128 rectangular grid cells with $\Delta x = 0.4$ and $\Delta z = 0.1$. We use the second order Lax–Friedrichs scheme, the MC limiter and $\beta = 1.2$. For the resistive MHD simulations (with no Hall term) the resistivity is set to $\eta = 0.005$. In the Hall MHD runs the resistivity is the same and the normalized ion mass per charge is 1. Fig. 6 shows the time dependence of the reconnected flux $\int_0^{L_x/2} B_z dx$ for classical resistive and Hall MHD simulations. The results agree quite well with Fig. 1 in Birn et al. [3] despite the split reconnection site in the Hall MHD simulation. We checked that starting with a larger perturbation results in a single reconnection site and the reconnection rate remains about the same.
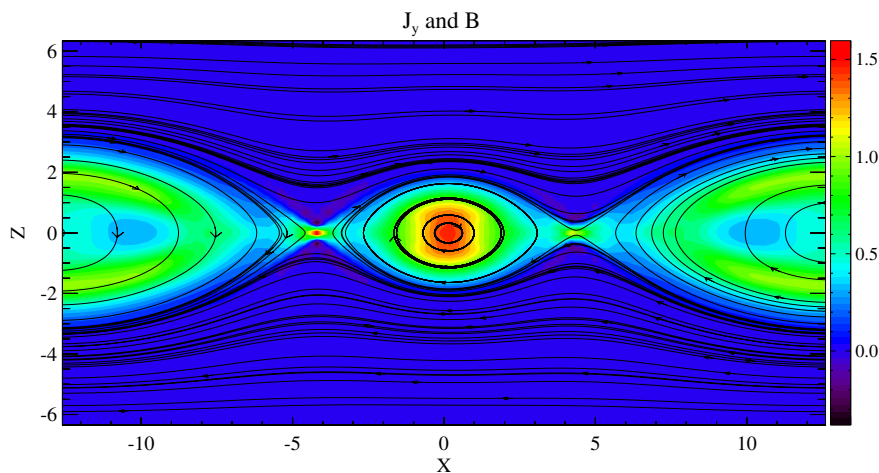

Fig. 5. The current (color) and some magnetic field lines at $t = 30$ for the Hall MHD simulation of the GEM reconnection problem.
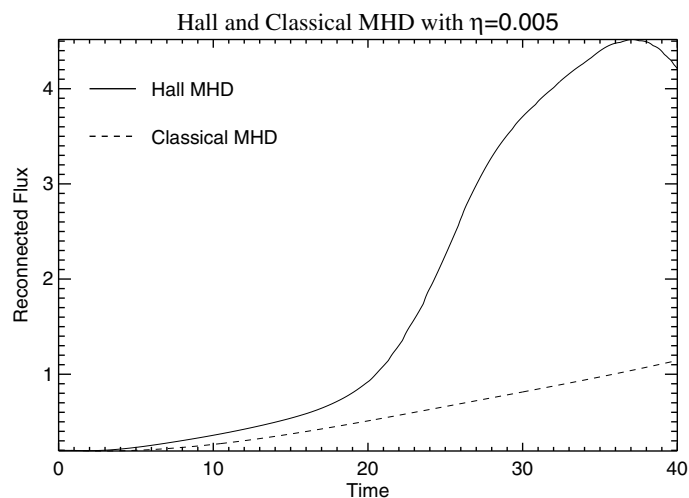

Fig. 6. The reconnected magnetic flux versus time for constant resistivity in the GEM reconnection problem.

4.3. Three-dimensional magnetosphere simulations and parallel scaling

Finally, we tested if the code gives physically reasonable results for magnetosphere type problems. We are solving the flow of the solar wind around the Earth. The solar wind flows in the x direction, the dipole is aligned with the z direction, and the magnetic field of the solar wind has a pure B_z component only that is opposite of the orientation of the dipole field in the equatorial plane. For classical MHD the solution is perfectly symmetric in the $\pm Z$ and $\pm Y$ directions. For Hall MHD we expect the solution to be asymmetric which means that B_y can be non-zero in the $Y = 0$ plane.

Fig. 7 shows the magnetosphere solution together with the grid structure in the $Y = 0$ plane. Both the dayside (left of the body) and the magnetotail reconnection regions are highly resolved with $1/32 R_E$ (Earth radii)
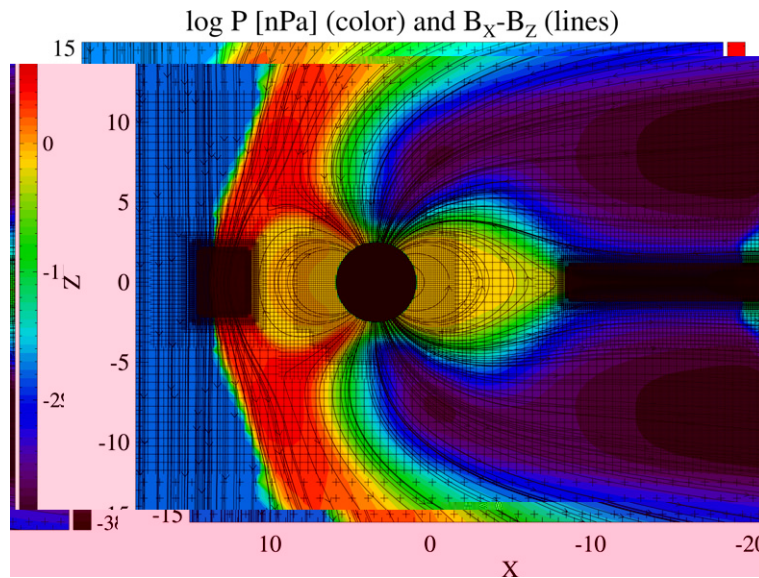

Fig. 7. Magnetosphere solution in the $Y = 0$ plane. The black crosses show the grid cell centers. Distance is measured in Earth radii.
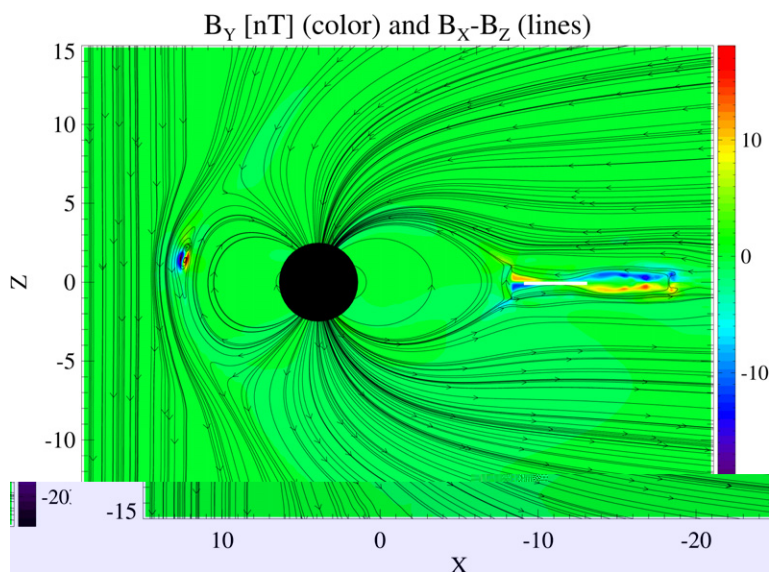

Fig. 8. Magnetosphere field solution with Hall MHD. Note the quadrupolar B_y field in the tail.

cells. There are 71,000 $4 \times 4 \times 4$ grid blocks with more than 4.5 million cells altogether. Fig. 8 shows the solution obtained with local time stepping. The B_y component has the typical quadrupolar structure at the magnetotail. The day-side reconnection site moved northward which suggests that the solution is unstable. This is most likely a particular manifestation of the tearing mode instability, also known as Flux Transfer Events (FTE) in the space physics literature (e.g. [18]). The presence of this instability as well as the lack of perfect convergence of the local time stepping scheme suggests that the solution is time dependent despite the fixed boundary conditions.

We have repeated the simulation in time dependent mode with a slightly reduced resolution. The grid consists of 4848 blocks of size $8 \times 8 \times 8$ cells, or about 2.5 million cells altogether. The cell sizes range from 8 to 1/ $16 R_E$. The high resolution is concentrated around the reconnection region in the magnetotail and Hall MHD is solved in this region only. Outside this region the Hall term is neglected. In this time accurates simulation we have indeed found that the solution shows a quasi-periodic behavior with periodic plasmoid formation. The physical interpretation of these results are outside the scope of this paper, on the other hand this rather expensive simulation provides an excellent demonstration of the parallel scaling and efficiency of the explicit and implicit Hall MHD schemes.

We present scaling results on an SGI Altix super computer (columbia at NASA Ames) for short runs (25 s) starting from a restart file saved at about 2 h simulation time. Fig. 9 shows scaling curves for explicit, implicit and explicit/implicit time stepping, respectively. For the explicit scheme the stability condition required $\Delta t = 0.00295$ s time steps, while the time step for the implicit scheme was 1 s. The figure demonstrates a near perfect scaling of the explicit scheme from 32 to 1616 processors, which is quite remarkable for strong scaling with a fixed problem size. Note that there are only 3 blocks per processor when the code runs on 1616 processors.

The fully implicit and explicit/implicit algorithms are about 14 and 20 times faster on 32 CPU-s than the explicit scheme, respectively. The implicit time step is about 330 times larger than the explicit time step, and the implicit scheme requires about 25 Krylov iterations per step. The Krylov iterations are less expensive than the full explicit time step, because the Jacobian-free evaluation uses the first order scheme (no limiters), but the construction and application of the preconditioner also takes up significant time. The overall gain of the fully implicit scheme over the explicit scheme happens to be close to the simple estimate of $330/25 = 13.2$.
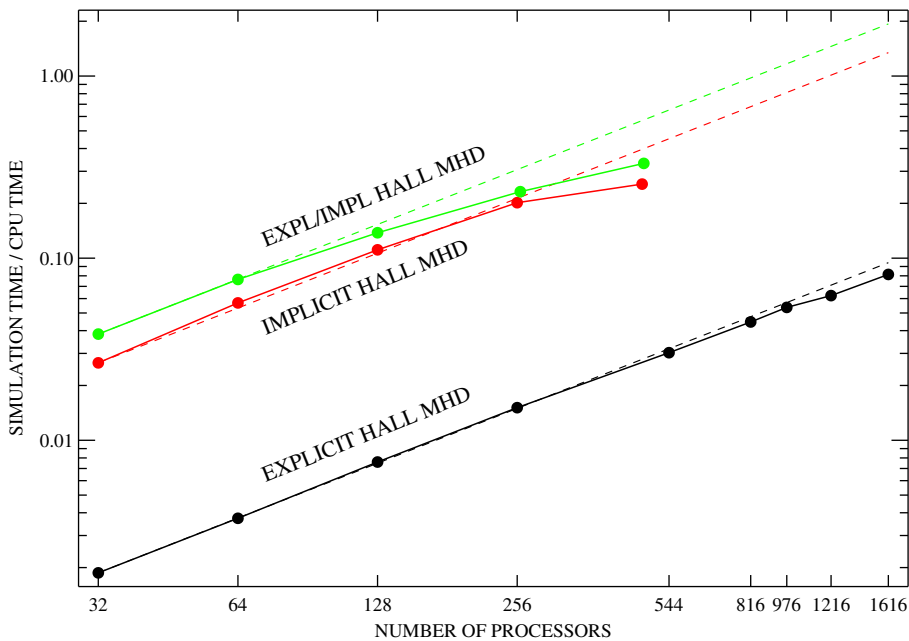

Fig. 9. Scaling of the explicit, implicit and explicit/implicit time stepping schemes for a fixed size magnetosphere problem.

As the figure shows the implicit schemes scale quite well up to 256 processors. In the explicit/implicit scheme most of the blocks (about 3400) require implicit time steps for the selected time step, so there is relatively little difference between the efficiency of the implicit and explicit/implicit algorithms.

5. Conclusions

We have developed a second order accurate Hall MHD scheme for block adaptive Cartesian or general structured grids using both explicit and implicit time integration. For steady state solutions the explicit scheme can be used in combination with local time stepping. Care should be taken to use symmetric type limiters (like MC) instead of asymmetric limiters (like minmod or super-bee) to achieve second order accuracy in smooth regions. For time accurate runs the implicit scheme is much more efficient than the explicit scheme if the whistler wave speed is dominant. The preconditioner has to take into account the terms responsible for the whistler wave. Using the implicit scheme the Hall MHD simulation ran about 3–4 times slower than the classical MHD simulation, which is quite reasonable given the stiffness of the Hall MHD equations due to the whistler wave.

The efficiency and good parallel scaling of our Hall MHD scheme enables us to do steady state and time accurate simulations in three-dimensional. We have already used the Hall MHD code to simulate Titan's interaction with the surrounding plasma [10]. This steady state simulation uses a spherical grid with logarithmic stretching in the radial direction. As shown by Ma et al. [10] the Hall MHD results match the values measured by the Cassini satellite significantly better than the results obtained with classical MHD simulations. We plan to use the Hall MHD code to study many space physics problems in the future.

While Hall MHD captures the most important kinetic effects, it does not describe the full physics. Comparing Hall MHD and hybrid model results [24,6,23], it was found that the off-diagonal elements of the pressure tensor play an important role. We plan to extend our code to use a non-isotropic pressure equation with field-aligned and orthogonal components. We are also working on extending our code to multi-fluid Hall MHD with ions of different mass.

Acknowledgements

References

[1] M.J. Berger, P. Colella, Local adaptive mesh refinement for shock hydrodynamics, J. Comput. Phys. 82 (1989) 67–84.

[2] A. Bhattacharjee, K. Germaschewski, C.S. Ng, Current singularities: drivers of impulsive reconnection, Phys. Plasmas 12 (2005).

[3] J. Birn, J.F. Drake, M.A. Shay, B.N. Rogers, R.E. Denton, M. Hesse, M. Kuznetsova, Z.W. Ma, A. Bhattacharjee, A. Otto, P.L. Pritchett, Geospace environmental modeling (GEM) magnetic reconnection challenge, J. Geophys. Res. 106 (A3) (2001) 3715–3720.

[4] L. Chacón, D.A. Knoll, A 2D high-β Hall MHD implicit nonlinear solver, J. Comput. Phys. 188 (2003).

[5] P. Dmitruk, W.H. Matthaeus, Structure of the electromagnetic field in three-dimensional hall magnetohydrodynamic turbulence, Phys Plasmas 13 (2006).

[6] M. Hesse, J. Birn, M. Kuznetsova, Collisionless magnetic reconnection: electron processes and transport modeling, J. Geophys. Res. 106 (A3) (2001) 3721–3736.

[7] J.D. Huba, A new 3D Hall MHD code, in: J. Büchner, C.T. Dum, M. Scholer (Eds.), Proceedings of Sixth International School/Symposium on Space Plasma Simulation, Copernicus Gesellschaft, Garching, 2001, pp. 143–146.

[8] J.D. Huba, Hall magnetohydrodynamics – a tutorial, in: J. Büchner, C.T. Dum, M. Scholer (Eds.), Space Plasma Simulation, Springer-Verlag, Berlin, 2003, pp. 166–192.

[9] B. Koren, A robust upwind discretisation method for advection, diffusion and source terms, in: C.B. Vreugdenhil, B. Koren (Eds.), Numerical Methods for Advection–Diffusion Problems, Vieweg, Braunschweig, 1993, p. 117.

[10] Y.J. Ma, A.F. Nagy, G. Tóth, T.E. Cravens, C.T. Russell, T.I. Gombosi, J-E. Wahlund, F.J. Crary, A.J. Coates, C.L. Bertucci, F.M. Neubauer, 3D global multi-species Hall MHD simulation of the cassini t9 flyby, Geophys. Res. Lett. 34 (2007).

[11] P.D. Mininni, D.O. Gomez, Direct simulations of helical Hall MHD turbulence and dynamo action, Astrophys. J. 619 (2005) 1019–1027.

[12] L.F. Morales, S. Dasso, D.O. Gomez, Hall effect in incompressible magnetic reconnection, J. Geophys. Res. 110 (2005).

[13] F. Mozer, S. Bale, T.D. Phan, Evidence of diffusion regions at a subsolar magnetopause crossing, Phys. Rev. Lett. 89 (2002).
[14] M. Oieroset et al., In situ detection of collisionless reconnection in the earth's magnetotail, Nature 412 (2001).
[15] S. O'Sullivan, T.P. Downes, An explicit scheme for multifluid magnetohydrodynamics, MNRAS 366 (2006) 1329–1336, doi:10.1111/ j.1365–2966.2005.09898.x.
[16] A. Otto, Geospace environment modeling (gem) magnetic reconnection challenge: MHD and Hall-MHD constant and current dependent resistivity models, J. Geophys. Res. 106 (2001).
[17] K.G. Powell, P.L. Roe, T.J. Linde, T.I. Gombosi, D.L. De Zeeuw, A solution-adaptive upwind scheme for ideal magnetohydro- dynamics, J. Comput. Phys. 154 (1999) 284–309.
[18] J. Raeder, Flux transfer events: 1. Generation mechanism for strong southward IMF, Ann. Geophys. 24 (2006) 381–392.
[19] Q.F. Stout, D.L. De Zeeuw, T.I. Gombosi, C.P.T. Groth, H.G. Marshall, K.G. Powell, Adaptive blocks: a high-performance data structure, in: Proceedings of Supercomputing'97, 1997.
[20] T. Tanaka, Finite volume TVD scheme on an unstructured grid system for three-dimensional MHD simulations of inhomogeneous systems including strong background potential field, J. Comput. Phys. 111 (1994) 381–389.
[21] G. Tóth, D.L. De Zeeuw, T.I. Gombosi, K.G. Powell, A parallel explicit/implicit time stepping scheme on block-adaptive grids, J. Comput. Phys. 217 (2006) 722–758.
[22] B. van Leer, Towards the ultimate conservative difference scheme. V. A second-order sequel to Godunov's method, J. Comput. Phys. 32 (1979) 101–136.
[23] L. Yin, D. Winske, Simulations of current sheet thinning and reconnection, J. Geophys. Res. 107 (A12) (2002).
[24] L. Yin, D. Winske, S.P. Gary, J. Birn, Hybrid and Hall-MHD simulations of collisionless reconnection: dynamics of the electron pressure tensor, JGR 106 (A6) (2001) 10,761–10,776.
[25] Z. Ma, A. Bhattacharjee, Hall magnetohydrodynamic reconnection: the geospace environment modeling challenge, JGR (2001) 106.